Proceedings of the Institute of Acoustics

CORRECTION OF APERTURE ERRORS IN CIRCULAR SAS IMAGERY VIA PSEUDO-STRIPMAP AUTOFOCUSING

T. M. Marston APL-UW, Seattle, Washington, 98105 USA
J. L. Kennedy NSWC PCD, Panama City Beach, Florida, 32407 USA
J. L. Prater NSWC PCD, Panama City Beach, Florida, 32407 USA

1 INTRODUCTION

Circular synthetic aperture imaging is a challenging mode of synthetic aperture processing, even for airborne systems employing GPS. Examples in radar and sonar literature[1,2,3] often include artificially introduced isotropic scatterers or active beacons to serve as focusing references. Though effective, the necessity for isotropic scatterers is a major handicap, especially underwater. Data driven alternatives for estimating phase error have been proposed[4,5]. These methods are very efficient and require only one instance of beamforming, however spatial invariance of focus aberrations is an implicit assumption. Another proposed method[6] can theoretically compensate for spatial variance, however it is more computationally expensive and requires manual specification of control-points.

This paper describes a method for creating aperture corrections that does not implicitly assume spatial invariance. Rather, it utilizes spatial variance to differentiate between aperture error types in a framework that is both efficient and robust. The algorithm operates on a pseudo-stripmap image generated using a single convolution operation in the angular dimension. An estimate of the range-variant quadratic error as a function of aperture angle is used to invert relevant aperture corrections. The range-variances of a variety of errors are calculated and the error inversion process tested on real circular synthetic aperture sonar (CSAS) data.

2 PSEUDO-STRIPMAP IMAGING

Algorithms for imaging scatterers on rotating platforms (analogous to CSAS imaging) appear in early radar literature[7] and the pseudo-stripmap imaging algorithm in this paper will take a similar approach. Consider the circular aperture scenario illustrated in Figure 1.

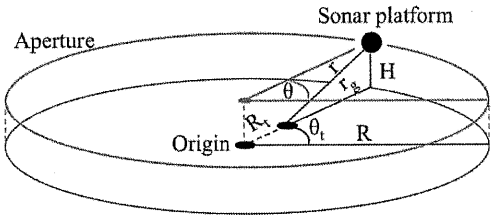

Figure 1: CSAS aperture geometry in cylindrical coordinates. Distances from the origin are denoted using capital R, (e.g. R = aperture radius, R_t = target radius). Distances from the platform at the location of closest approach are labelled using lowercase r, (e.g. r = slant-plane, r_g = ground-plane).

The distance between an arbitrary point and the source traveling along the aperture is:

, (1)

where D is the distance between source and scatterer, R is trajectory radius, R_t is scatterer radius, H is platform height, θ is the angular location of the sonar around the aperture, and θ_t is the angular orientation of the scatterer. This distance formula will be expanded about $\theta = 0$, the angle of minimum or maximum distance for the case that $\theta_t = 0$. Because the signal originates from the sonar platform it can be helpful to make the substitution $R_t = (R - (r^2-H^2)^{1/2})$ where r is slant range to the target at $\theta = \theta_t = 0$. With this substitution the second order expansion is:

. (2)

The range-dependent quadratic coefficient describes the curvature of at its apex. This curvature is used to define the phase of an azimuthal chirp exploited by pseudo-stripmap imaging to provide azimuthal compression. For efficiency (at the price of azimuthal resolution) it is applied as a one-dimensional convolution operation in θ. To do this an envelope function must be generated that truncates the chirp at the θ value corresponding to when the delay difference from the apex exceeds one range-cell. For a monostatic system with a given bandwidth, a range-cell spans $\Delta R = c/(2*f_{BW})$. A pair of sigmoid functions can be used to mask the azimuthal chirp by the range-cell constraint:

, (3)

where controls the sharpness of the cutoff and is the cutoff angle corresponding to the θ value at which the delay from the apex equals ΔR. The frequency domain representation of the chirp with the included envelope function can be calculated directly via the principle of stationary phase[8]:

. (4)

This is the angular wavenumber expression, including bandwidth gating, for the azimuthal chirp used to compress the raw data in . The bandwidth of is determined by the cutoff of. Substituting into the envelope function of Eq. (3), the range-variant cutoff wavenumber can be calculated in the positive and negative wavenumber directions:

. (5)

From Eq.'s (2) and (5) it can be seen that the resolution of pseudo-stripmap images generated using decrease as $|r_g - R|$ decreases. Additionally, the azimuthal bandwidth of is contingent on ΔR. By reducing temporal bandwidth the azimuthal bandwidth can be enlarged, enabling to a limited degree the ability to trade temporal resolution for resolution in .

Figure 3 shows an example psudeo-stripmap image from a synthetic aperture sonar system mounted on a UUV:

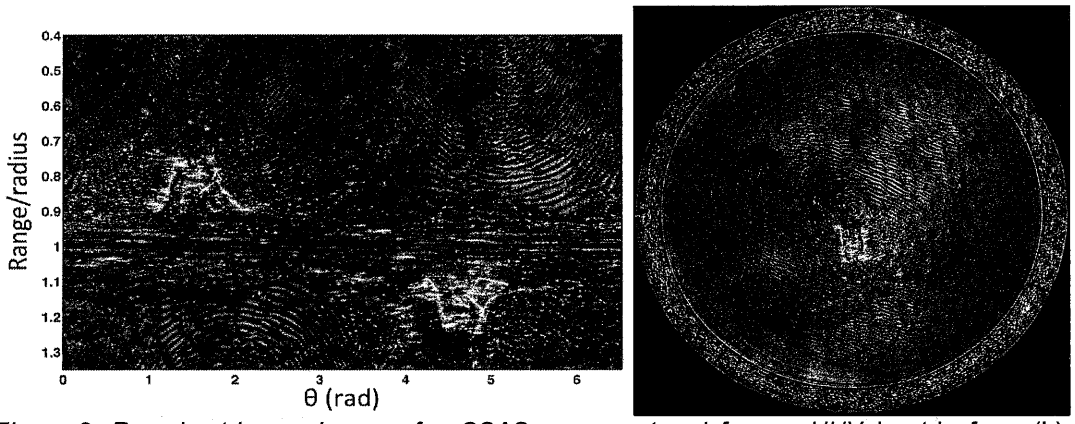

Figure 2. Pseudo-stripmap image of a CSAS scan captured from a UUV in strip form (L) and interpolated to a Cartesian grid (R). The figure at right is generated using ranges spanning from 0 to the radius. A similar image can be generated using ranges greater than and equal to the radius.

Consistent with Eq. (5) the pseudo-strip map image in Fig. 2 (L) shows reduced resolution in in the vicinity of $r \approx r_g = R$.

Aperture distortions cause local inaccuracies in the model that can be defined as parameter perturbations. The difference between the assumed model and a model incorporating a perturbation defines the range-variant phase error:

, (6)

where

. (7)

In the previous expression ζ defines the range variant quadratic error component and is modified by a parameter perturbation. The following section shows ζ linearized for various parameter errors.

3 ERROR RANGE VARIANCE

This section shows the quadratic error range variance of Eq. (7) linearized for various perturbations of in cylindrical coordinates (angular error, radial error and height error), and propagation speed.

3.1.1 Angular Sampling Error

A local angular sample rate error occurring in the vicinity of some angle θ can be expressed:

. (8)

Substituting into Eq. (2), solving for modified quadratic coefficient and substituting into ζ,

. (9)

3.1.2 Radial Error

Small curvature deviations can be modeled by a change in the radius of the circular aperture, = (1+)R where << 1. The resulting -function is:

. (10)

Neglecting higher order terms, substituting the change in radius ΔR with R and linearizing yields:

. (11)

3.1.3 Height Error

A local height error at θ can be modeled as =(1+)H:

. (12)

Neglecting second and higher order μ-terms, setting ΔH = μH and linearizing,

. (13)

3.1.4 Propagation Speed Error

Propagation speed errors alter phase curvature by affecting k in Eq. (6): . This can be incorporated into the modified β-function:

. (14)

Substituting into Eq. (7) and simplifying yields:

. (15)

It is apparent from Eq. (9) and (15) that sample rate and propagation speed range variances are scaled versions of the same expression. Based on an assumption that propagation speeds can be accurately measured and will likely not vary significantly over the scale of the aperture, ζ_{prp} will be neglected. The derived error range variances are plotted in Figure 3.

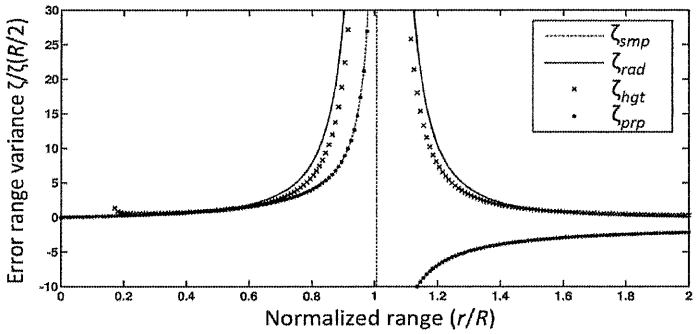

Figure 3. Range variance of quadratic phase errors for angular sample rate errors (ζ_{smp}), radius errors (ζ_{smp}), height errors (ζ_{smp}), and propagation speed errors (ζ_{smp}). The curves have been normalized by the half-radius value.

Transducer beamwidth limitations can reduce the available radius for full-aperture CSAS data processing to the region in the vicinity of r = R. Near this region ζ_{rad} and ζ_{hgt} are difficult to discriminate, especially for low-grazing angle scenarios, and it is practical to lump both types of errors into one correction. In subsequent examples ζ_{rad} and ζ_{smp} are the only expressions used for inversion.

4 LOCAL QUADRATIC ERROR ESTIMATION

The well-known mapdrift algorithm can be used to measure quadratic phase error and provides a good balance between robustness and efficiency. Mapdrift operates by dividing an aperture into two sub-apertures. The relative translation between images formed using disparate sub-apertures can be found via intensity image correlation and, in conjunction with azimuthal bandwidth, may be used to estimate quadratic error[9, 10].

When applied to a pseudo-stripmap scenario, sub-apertures are formed by windowing the angular spectrum. The estimation of quadratic error range variance at some aperture location θ_n can be found by measuring the *local* (i.e. in the vicinity of θ_n) translation in the θ direction between pseudo-stripmap sub-aperture images. Because the bandwidth is range variant (Eq. (5)) this implies an additional bandwidth factor will modify the previously calculated range variances. Assume two sub-apertures are generated by windowing the spectrum from $-k_{\theta\_ctf}$ to 0 in one case and 0 to k_{θ_ctf} in the other. The translational shift induced by quadratic error is found using the derivative of the phase term in Eq. (4) with respect to k_θ and evaluating at $k_{\theta\_ctf}/2$:

. (16)

For a given angular sample rate this translation can be expressed in terms of a pixel shift:

. (17)

This image translation range variance function can be thought of as the quadratic phase error range variance ζ modified to account for the range dependency of the image azimuthal bandwidth.

5 ERROR INVERSION AND CORRECTION

Local mapdrift results in an *MxN* measurement matrix $S(r,\theta)$ containing translation measurements that are assumed a-priori to be a summation of pairs of linearly independent functions and noise:

. (18)

The *M*-length column vectors $\xi_{smp}(r)$ and $\xi_{rad}(r)$ describe the range-variance of translational offsets induced by the quadratic errors for sample rate offsets and radial curvature errors. The coefficients $A(\theta)$ and $B(\theta)$ correspond to the respective contributions of each error at some aperture location θ. Matrix η represents noise that is not necessarily uniform in r or θ. If an estimate of η can be made (e.g. via correlation coefficient), a weighting matrix $w(r, \theta)$ can be generated to de-weight the portions of $S(r, \theta)$ that correspond to lower certainty. A weighted least-squares estimate of coefficients $A(\theta)$ and $B(\theta)$ can be found at θ_n via:

(19)

In Eq. (19) the symbol represents the Hadamard product. Outlier rejection can be enhanced by iteratively re-defining the weighting matrix. In the following tests *A* and *B* are iteratively solved for and used to generate a denoised reconstruction of $S(r,\theta)$. The weighting matrix is recalculated via:

, (20)

where *v* controls outlier rejection, *i* denotes iteration number and is the surface reconstructed from the functions and the i^{th} estimate of their coefficients. The result of error inversion is the pair of vectors *A* and *B* corresponding to curvature error and resampling error. Local curvature estimates can be related to the total radial error $\varepsilon_{rad}(\theta)$ error using a derived recursion relation for the circular aperture geometry[5]:

, (21)

where $\Delta\theta$ is the angular spacing between aperture samples. Initial conditions are necessary, however the values are arbitrary and result in a translation inducing first-order sinusoidal component that can be removed. For resampling errors the correction is found by integration:

. (22)

The radial errors are then applied via shifting data in range, and the sampling errors are applied by resampling to the new axis modified by ξ_{smp}. Ideally only a single iteration of the error-estimation and correction process is necessary, however results indicate that focus benefits from multiple iterations. Computational efficiency is retained if the iteration process is applied to data that has been decimated to remove angular spectral content beyond k_{θ_ctf}. After the final iteration the computed solution, including modifications from iteration, is up sampled and applied to the original raw dataset before image reconstruction.

6 APPLICATION AND RESULTS

To test that range-variances are being calculated correctly and are separable, a previously motion-compensated circular aperture dataset captured from an unmanned underwater vehicle (UUV) system is injected with angular sampling errors and radial errors. The injected errors are then compared with the estimated errors. The injected signals are tapered narrow-band signals having different frequencies, so that any cross-talk between error sources can be observed. A comparison of the injected error vs. recovered estimates is shown in Figure 4.

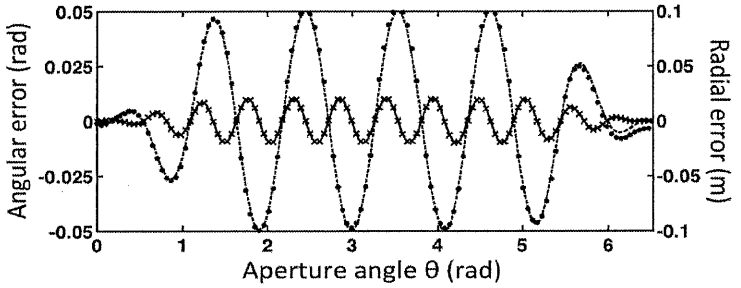

Figure 4: Inserted angular (solid line) and radial (dashed line) errors vs. measured angular (x's) and radial (dots) errors, estimated via application of local map-drift measurements to a pseudo-stripmap image and using range variance to invert error parameters. Five iterations were applied.

Results indicate that inserted errors are well recovered and show almost no cross talk. The algorithm was next applied to a dataset exhibiting residual motion error after initial redundant phase-center processing was applied for bulk error removal. Figure 5 show the range and angle variant quadratic phase error estimates before an after error estimation and correction.

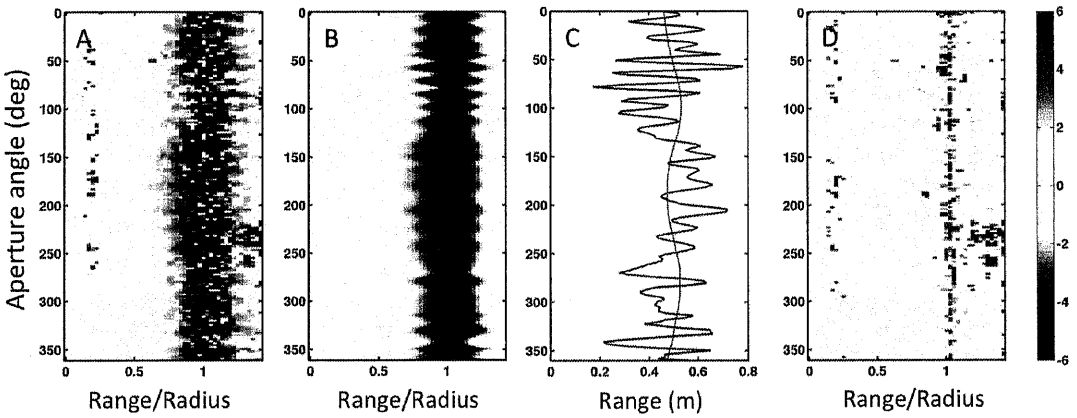

Figure 5: (A) Initial local translation estimates (color scale on the far right in units of pixels), (B) reconstructed shift surface using the coefficients from inversion, (C) local radial curvature (solid) and reconstructed range error (dotted) estimates, and (D) the flattened shift surface estimates after 5 algorithm iterations. Angular corrections were insignificant and not plotted in (C).

The images in Fig. 6 show the CSAS image generated with and without the correction.

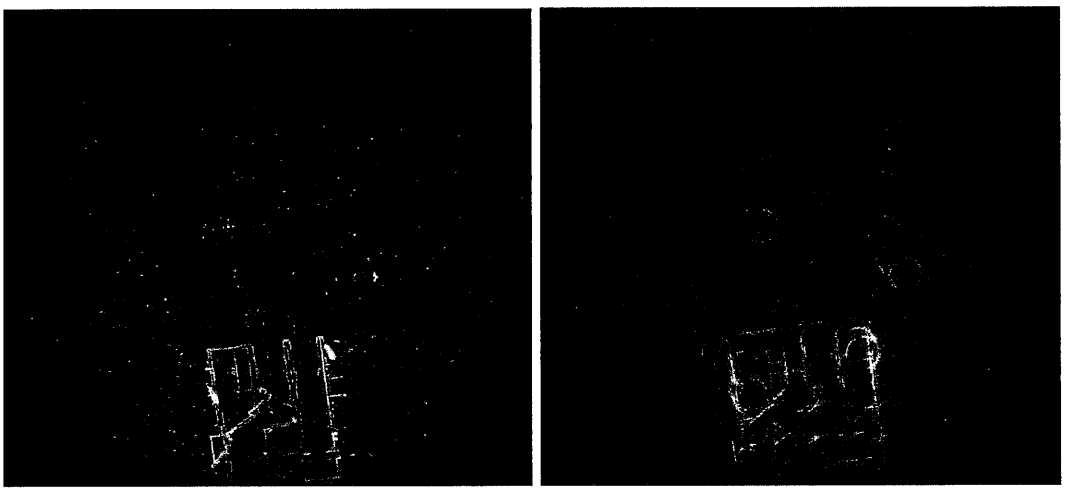

Fig. 6: CSAS image with (L) and without (R) aperture corrections for error inversion. The circular nature of the focusing aberrations shown in the right figure indicate that the dominant component of the defocusing error is a static height or radial error. This is consistent with the radial shift error plotted in Fig. 5(C).

7 CONCLUSION

A pseudo-stripmap image is formed by convolving circular aperture data in the angular dimension with a phase compression function derived from the quadratic expansion of the range-variant time delays to scatterers. This imaging method was found to be effective for estimating and correcting phase errors in circular synthetic aperture data. In the pseudo-stripmap domain the range variance of the quadratic errors induced by radial curvature and angular sampling errors have unique and separable signatures that can be estimated via the inversion methods described in Section V. Once estimated they can be applied directly to data for correction. The high level of azimuthal decimation that can be employed when generating pseudo-stripmap imagery means that local quadratic phase estimation, aperture error inversion, and correction can be completed efficiently. Two examples were given: one contained manually injected errors and one contained residual uncorrected phase errors after initial bulk phase error removal. In the first example the resulting corrections closely matched the injected errors. In the second example the local quadratic error estimations showed greatly reduced levels of error and the level of image focus showed excellent qualitative improvement.

8 ACKNOWLEDGEMENTS

This research was supported partially by the U.S. Department of Defense Strategic Environmental Research and Development Program (SERDP) and the Office of Naval Research (ONR).

9 REFERENCES

1. S. K. Mitchell, K. N. Scarbrough, S. P. Pitt, and T. L. Kooij, "High resolution circular SAS with controlled focus," Proceedings of the Institute of Acoustics, Vol. 28, p. 65 (2006).
2. C. H. Casteel, L. A. Gorham, M. J. Minardi, S. Scarborough, and K. D. Naidu, "A challenge problem for 2D/3D imaging of targets from a volumetric data set in an urban environment," in *Proc. SPIE 6568*, Apr 2007.
3. O. Ponce, P. Prats-Iraola, M. Pinheiro, M. Rodriguez-Cassola, R. Scheiber, A. Reigber, A. Moreira, "Fully Polarimetric High-Resolution 3-D Imaging with Circular SAR at L-band," IEEE Transactions on Geoscience and Remote Sensing, Vo. 52, pp. 3074-3090, (2013).
4. T. M. Marston, "A Correlation Based Autofocusing Algorithm for Coherent Circular Synthetic Aperture Sonar," Proceedings of the European Conference on Synthetic Aperture Radar (EUSAR), April 2012.
5. T. M. Marston, J. L. Kennedy and P. L. Marston, "Autofocusing Circular Synthetic Aperture Sonar Imagery Using Phase Corrections Modeled as Generalized Cones," [accepted for publication]
6. H. M. J. Cantalloube and C. E. Nahum, "Multiscale Local Map-Drift-Driven Multilateration SAR Autofocus Using Fast Polar Format Image Synthesis," IEEE Transactions on Geoscience and Remote Sensing," Vol. 49, pp. 3730-3736, (2011).
7. W. M. Brown, and R. J. Fredricks, "Range-Doppler imaging with motion through resolution cells," IEEE Transactions on Aerospace and Electronic Systems, vol. 5, no. 1, pp. 98-102, January 1969.

8. D. W. Hawkins, "Synthetic aperture imaging algorithms: with application to wide bandwidth sonar." Ph.D. dissertation, Department of Electrical and Electronic Engineering, University of Canterbury, Oct. 1996, (See Appendix A).
9. W. G. Carrare, R. S. Goodman, R. M. Majewski, "Spotlight Synthetic Aperture Radar: Signal Processing Algorithms." Artech House, 1995 (See chapter 6).
10. O.O. Bezvesilniy, I.M. Gorovyi and D.M. Vavriv, "Estimation of phase errors in SAR Data by local-quadratic map-drift autofocus", Proc. 13th Int. Radar Symp. IRS-2012, Warsaw, Poland, pp. 376-381, 2012.